curves of S versus V are highly reproducible and independent of voltage history. If there is any hysteresis, it is much less than 1 microstrain.

Two primary areas where STO may find application are in low-temperature actuators and magnetic field–insensitive thermometers. The most broadly used application for linear actuators is in cryogenic scanning probe microscopy (*16–19*). The linear (piezoelectric) region above V_c is most useful here. Operation would then be about a bias voltage, which near 4.2 K is only about $V_c = 25$ V. The absence of hysteresis also makes precise scanning simpler, although the temperature dependence of the effect would require significant temperature stabilization. The phase boundary separating quadratic from linear behavior is shown in Fig. 4. The crossover voltage decreases with T and shows no sign of flattening out. This effect is useful for linear applications, which would then require a smaller bias voltage at lower T. At V_c, the value of the strain S_c is actually increasing. Thus, any application that depends on the quadratic behavior continues to work as T is lowered but requires less voltage for the same response. Such applications might include acoustic generators (*20*), which would act as frequency doublers as a result of the quadratic response.

The divergence of the coefficients R and d may also be used as a thermometer. Because there are no spins or currents in STO at low temperatures, the main advantage of such a thermometer would be that it might be unaffected by a magnetic field, a very difficult property to achieve in cryogenic thermometry. A lock-in amplifier could be used with an ac applied voltage to continuously read the slope of the curve of S versus V. If a metal strain gauge were to be used (as in our experiment), although the resistance Ω may change in a magnetic field, the ratio $S = \Delta\Omega/\Omega$ would not change. Other methods of measuring the strain may be used as well. Given the apparent divergence of R, such a thermometer may work at temperatures far below what we have measured (*22*).

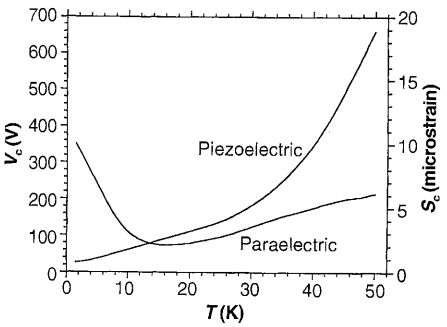

Fig. 4. The boundary between quadratic (PE) and linear (piezoelectric) behavior of the electric field–induced strain in STO shown as the value of the voltage V_c and strain S_c at the crossover as a function of temperature. At low temperatures S_c is increasing, implying that the PE region, which is useful in certain applications, persists to $T = 0$; the decreasing V_c shows that less voltage is required to reach the linear response regime (*21*).

REFERENCES AND NOTES

1. K. A. Waldner, W. Berlinger, F. Waldner, *Phys. Rev. Lett.* **21**, 814 (1968).
2. W. Zhong and D. Vanderbilt, *Phys. Rev. B* **53**, 5047 (1996).
3. B. Hehlen, A.-L. Pérou, E. Courtens, R. Vacher, *Phys. Rev. Lett.* **75**, 2416 (1995).
4. K. A. Müller and H. Burkard, *Phys. Rev. B* **19**, 3593 (1979).
5. G. Schmidt and E. Hegenbarth, *Phys. Status Solidi* **3**, 329 (1963).
6. H. Uwe and T. Sakudo, *Phys. Rev. B* **13**, 271 (1976).
7. Impurities (in parts per million) are as follows: Na < 2, K = 2, Al = 44, Si < 2, Ca = 14, Fe < 2, Ba = 19.
8. The index k goes from 1 to 6 to include the cases in which two orthogonal electric fields are applied, for example, $E_3^2 = E_3E_3$ and $E_4^2 = E_1E_3$ [see I. S. Zheludev, *Physics of Crystalline Solids* (Plenum, New York, 1971), vol. 2].
9. Because the linear regime occurs above a crossover field, it does not extrapolate to zero strain at zero field. Including the crossover fields, we have $S_{ij} \simeq S_{cij} + d_{kij}(E_j - E_{cj})$ (it is not exact because S_c and E_c are taken in the middle of the crossover). The main point is that the derivative of this form and Eq. 2 are both d_{kij}.
10. E. Sawaguchi and L. E. Cross, *Ferroelectrics* **2**, 37 (1971).
11. Y. Yamada and G. Shirane, *J. Phys. Soc. Jpn.* **26**, 396 (1969).
12. D. E. Grupp and A. E. Goldman, in preparation.
13. S. L. Sondhi, S. M. Girvin, J. P. Carini, D. Shahar, *Rev. Mod. Phys.*, in press. (available at http://xxx.lanl.gov at cond-mat/9609279).
14. E. Sawaguchi, A. Kikuchi, Y. Kodera, *J. Phys. Soc. Jpn.* **18**, 459 (1963).
15. K. A. Müller, W. Berlinger, M. Capizzi, H. Gränicher, *Solid State Commun.* **8**, 549 (1970).
16. G. Meyer, *Rev. Sci. Instrum.* **67**, 2960 (1996).
17. J. Siegel, J. Witt, N. Venturi, S. Field, *ibid.* **66**, 2520 (1995).
18. F. Mugele, C. Kloos, P. Leiderer, R. Moller, *ibid.* **67**, 4880 (1996).
19. J. A. Helfrich, S. Adenwalla, J. B. Ketterson, *ibid.* **66**, 4880 (1995).
20. I. C. Manzanares, N. Mina-Camilde, A. Brook, J. Peng, V. M. Blunt, *ibid.*, p. 2644.
21. The high-field regime is labeled piezoelectric and not FE because it is possible that noncentrosymmetric systems exhibiting piezoelectricity may not be FE. This question might be resolved by low-temperature measurements in an electric field of the crystal structure or polarization. Although data relating to the latter are in the literature, further experiments are needed to firmly establish the existence of a high-field FE state in STO [see J. Hemberger, P. Lunkenheimer, R. Viana, R. Böhmer, A. Loidl, *Phys. Rev. B* **52**, 13159 (1995)].
22. Some years ago, W. N. Lawless [*Ferroelectrics* **7**, 379 (1974)] developed an STO glass-ceramic that has been used as a low-temperature, magnetic field–insensitive capacitance thermometer because its dielectric constant is temperature-dependent. The proposed STO strain thermometer may ultimately be more useful because of the apparent divergence of the strain with decreasing temperature. The dielectric constant of $SrTiO_3$ glass is not strongly temperature-dependent at the lowest temperatures.

23. Supported in part by NSF under grant NSF/DMR-9623477.

26 December 1996; accepted 20 February 1997

Primary Production in Antarctic Sea Ice

Kevin R. Arrigo,* Denise L. Worthen, Michael P. Lizotte, Paul Dixon, Gerhard Dieckmann

A numerical model shows that in Antarctic sea ice, increased flooding in regions with thick snow cover enhances primary production in the infiltration (surface) layer. Productivity in the freeboard (sea level) layer is also determined by sea ice porosity, which varies with temperature. Spatial and temporal variation in snow thickness and the proportion of first-year ice thus determine regional differences in sea ice primary production. Model results show that of the 40 teragrams of carbon produced annually in the Antarctic ice pack, 75 percent was associated with first-year ice and nearly 50 percent was produced in the Weddell Sea.

Sea ice surrounding the Antarctic continent varies in extent from 4×10^6 km^2 in summer to 20×10^6 km^2 in winter (*1*) and represents one of the largest and most dynamic ecosystems on Earth. Algae associated with ice may attain standing crops with amounts of chlorophyll a in excess of 400 mg m^{-2} and rates of primary production of >1 g C m^{-2} day^{-1}, comparable to productive oceanic regions (*2*, *3*). Because sea ice microalgal production is spatially and temporally variable, its contribution to the carbon cycle of the Southern Ocean and its importance as a food source for higher trophic levels [such as overwintering juvenile krill (*4*)] have been difficult to determine.

We used an expanded version of a one-

K. R. Arrigo, NASA Oceans and Ice Branch, Goddard Space Flight Center, Code 971.0, Greenbelt, MD 20771, USA.
D. L. Worthen, Science Systems and Applications Inc., Lanham, MD 20706, USA.
M. P. Lizotte, Department of Biology and Microbiology, University of Wisconsin–Oshkosh, Oshkosh, WI 54901, USA.
P. Dixon, Scripps Institution of Oceanography, University of California, San Diego, La Jolla, CA 92093, USA.
G. Dieckmann, Alfred-Wegener Institut für Polar- und Meeresforschung, Columbusstrasse, D-27570 Bremerhaven, Germany.

*To whom correspondence should be addressed.

dimensional numerical model (*5–7*) to investigate the dynamics of primary production in Antarctic pack ice between 1 October 1989 and 30 April 1990. This approach allowed us to resolve regional differences in the size of the sea ice algal standing crop and in the rate of carbon fixation as a function of sea ice type (first-year and multiyear ice), sea ice habitat (infiltration and internal freeboard layers), and environmental conditions. In the model, algae grow within an infiltration layer located at the sea ice-snow interface and within an internal freeboard layer near sea level. Nutrient exchange is a function of surface flooding and sea ice porosity (*8*). Algal growth in the bottom ice layer is neglected because this community is generally absent in pack ice (*9*). As input, the model uses measurements collected remotely (sea ice extent and snow thickness) and in situ (cloud cover and air temperature) (*10*). Simulations of sea ice in the Weddell Sea produced algal standing crops that compare favorably with in situ observations (Fig. 1); consequently, the model was extended to the entire Antarctic ice pack.

In the model, regional differences in primary production (Fig. 2) were largely determined by variations in the proportion of first-year ice. Although production within the freeboard layer of both ice types was similar and showed little spatial variation (*11*), annual production in the first-year infiltration layer was 27 times that in multiyear ice (Table 1). The highest rates of production were associated with those regions that had the highest

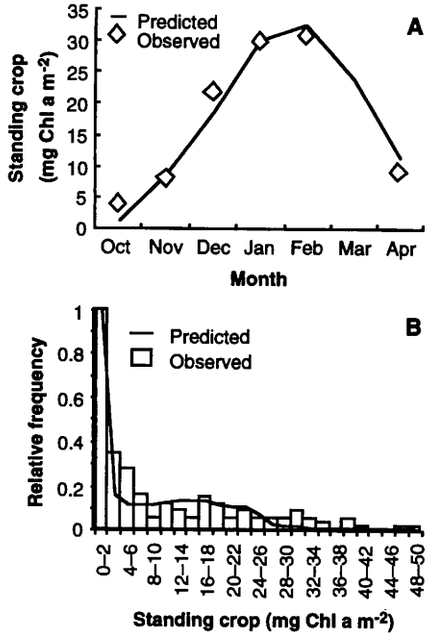

Fig. 1. (**A**) Mean monthly ice algal standing crop for the Weddell Sea predicted by the model and measured in sea ice cores (n = 257). In both cases the SDs were similar in magnitude and were approximately equal to the monthly means. (**B**) Frequency histograms for data used to generate (A). Chl a, chlorophyll a.

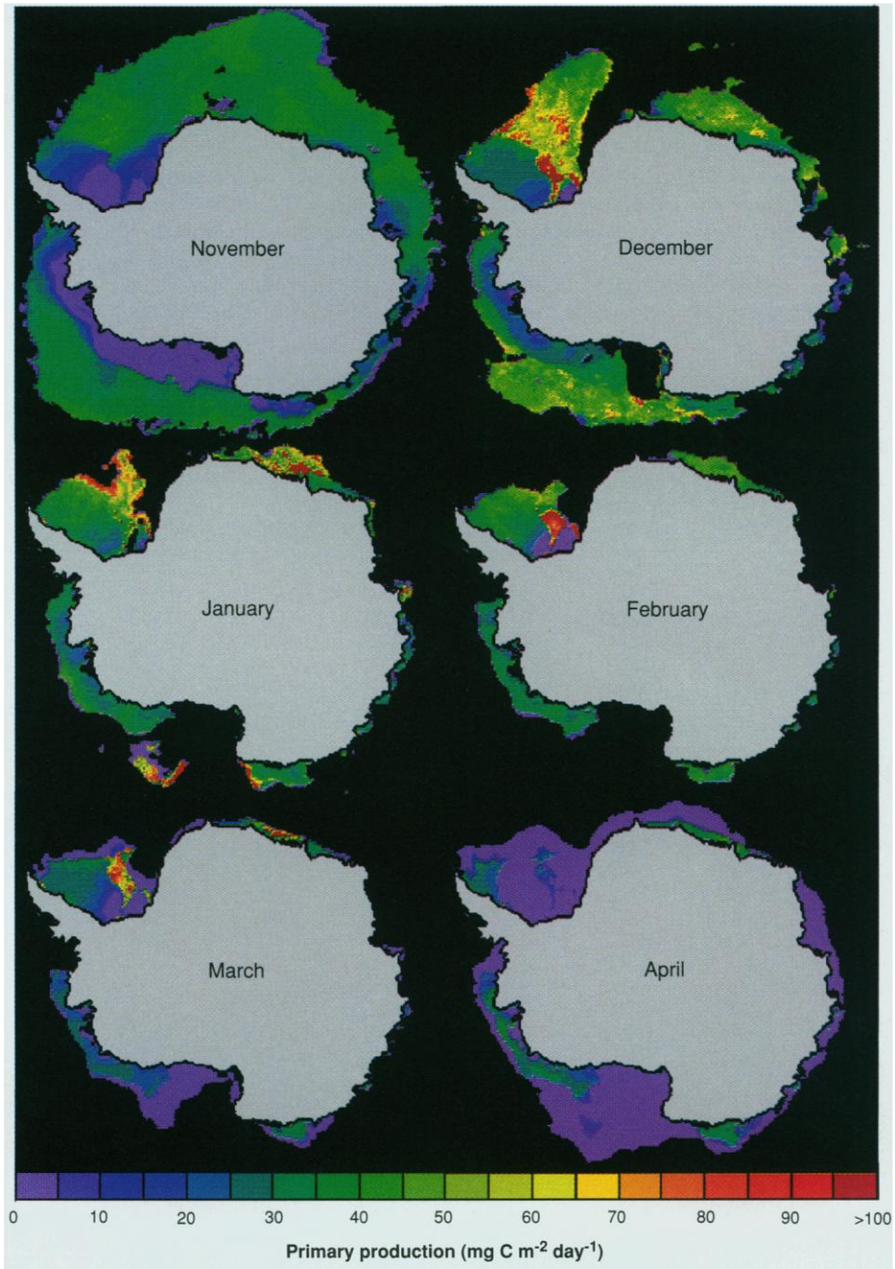

Fig. 2. Maps of sea ice primary production for the 15th day of each month during the simulation (October is not shown). Gray areas on the inset map denote multiyear ice.

proportion of first-year ice, such as the Weddell Sea (0.95 g C m^{-2} $month^{-1}$) and the southern Indian Ocean (1.02 g C m^{-2} $month^{-1}$). Productivity in these regions also was enhanced by thick mean snow cover (0.17 m) and high seawater nitrate concentration (23 μM). In contrast, in the southwestern Pacific, the transience of first-year ice and high proportion of multiyear ice (40 to 65%), thinner mean snow cover (0.13 m), and lower seawater nitrate concentration (18 μM) resulted in the lowest mean rate of production (0.59 g C m^{-2} $month^{-1}$) of any Antarctic region (Table 1).

The relative importance of light and nutrients for algal productivity throughout the Antarctic ice pack varied markedly with season and habitat. In the freeboard layer during the spring, algal biomass, productivity (Fig. 3A), and nutrient uptake were low, and algal growth was controlled by light availability (Fig. 3B). Increased amounts of light in November led to a marked rise in productivity; however, the concomitant increase in nutrient demand and reduction in nutrient concentrations limited algal growth during the austral summer. As temperatures cooled in late February (Fig. 3C), sea ice porosity decreased below the threshold required for nutrient exchange (8), resulting in a rapid decline in production within the freeboard layer (Fig. 3A). The timing of this decline varied spatially by more than 1 month (Fig. 3A) because of temperature differences. Because of its more restricted nutrient supply, the infiltration layer exhibited rates of primary production that peaked 1 to 2 months later than in the freeboard layer (Fig. 3D) (8). In the infiltration layer, light availability exceeded de-

Table 1. Temporal changes in first-year ice extent (FIE), productivity in the infiltration layer (PIF) and freeboard layer (PFF) of first-year ice, multiyear ice extent (MIE), productivity in the infiltration layer (PIM) and freeboard layer (PFM) of multiyear ice, and mean productivity for both ice types together (TPP).

Month	FIE (10^6 km^2)	PIF (g C m^{-2} $month^{-1}$)	PFF (g C m^{-2} $month^{-1}$)	MIE (10^6 km^2)	PIM (g C m^{-2} $month^{-1}$)	PFM (g C m^{-2} $month^{-1}$)	TPP (g C m^{-2} $month^{-1}$)
			Weddell Sea				
Oct	4.893	0.003	0.233	0.953	<0.001	0.031	0.203
Nov	4.174	0.036	0.985	0.919	0.001	0.369	0.903
Dec	2.055	0.533	1.163	0.900	0.016	0.851	1.443
Jan	0.662	1.729	1.140	0.844	0.043	1.077	1.899
Feb	0.401	1.353	0.674	0.760	0.049	0.910	1.328
Mar	0.629	0.470	0.305	0.722	0.027	0.656	0.726
Apr	1.357	0.033	0.120	0.719	0.005	0.218	0.177
							Mean = 0.953
			Southern Indian Ocean				
Oct	3.451	0.002	0.188	0.249	0.001	0.203	0.191
Nov	2.547	0.015	0.989	0.238	0.002	0.865	0.993
Dec	0.936	0.261	1.142	0.191	0.016	1.100	1.355
Jan	0.327	1.108	1.158	0.153	0.064	1.143	1.929
Feb	0.155	0.849	1.010	0.106	0.069	1.148	1.599
Mar	0.161	0.219	0.424	0.066	0.066	1.269	0.844
Apr	0.566	0.007	0.119	0.055	0.009	1.116	0.214
							Mean = 1.018
			Southwest Pacific Ocean				
Oct	0.601	0.002	0.119	0.413	<0.001	0.091	0.109
Nov	0.545	0.012	0.623	0.366	0.002	0.647	0.641
Dec	0.230	0.074	0.572	0.259	0.008	1.037	0.857
Jan	0.142	0.130	0.619	0.198	0.014	1.078	0.949
Feb	0.079	0.076	0.450	0.138	0.009	1.050	0.866
Mar	0.225	0.018	0.215	0.094	0.001	1.143	0.503
Apr	0.586	0.002	0.120	0.090	<0.001	0.678	0.196
							Mean = 0.589
			Ross Sea				
Oct	3.065	0.003	0.239	0.875	<0.001	0.115	0.214
Nov	2.343	0.024	0.928	0.855	0.003	0.308	0.781
Dec	1.446	0.235	1.159	0.712	0.015	0.920	1.243
Jan	0.367	0.581	0.844	0.370	0.034	1.017	1.237
Feb	0.106	0.074	0.377	0.268	0.006	0.947	0.811
Mar	0.750	0.004	0.100	0.222	<0.001	0.813	0.266
Apr	1.953	<0.001	0.054	0.221	<0.001	0.567	0.106
							Mean = 0.665
			Bellingshausen-Amundsen Seas				
Oct	1.371	0.001	0.111	0.474	<0.001	0.031	0.092
Nov	1.191	0.012	0.772	0.462	0.002	0.261	0.638
Dec	0.518	0.143	0.982	0.442	0.012	0.732	0.950
Jan	0.248	0.256	0.844	0.395	0.011	0.912	0.992
Feb	0.125	0.155	0.604	0.296	0.003	0.885	0.850
Mar	0.203	0.021	0.170	0.241	<0.001	0.935	0.595
Apr	0.437	0.001	0.076	0.233	<0.001	0.694	0.292
							Mean = 0.630

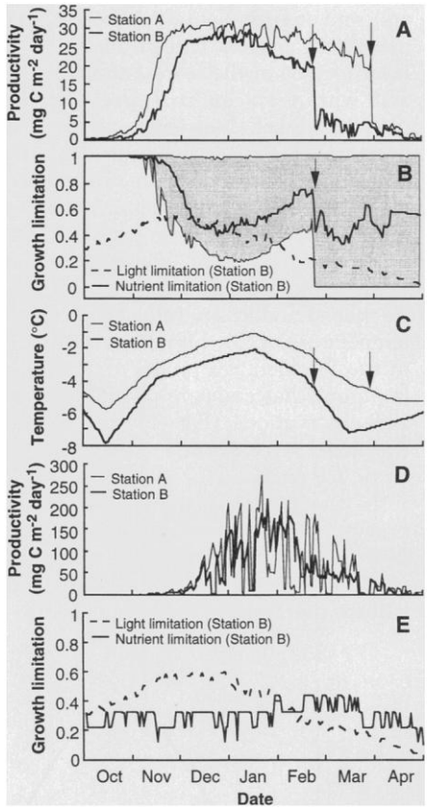

Fig. 3. (**A**) Modeled primary production in the freeboard layer at station A (71.4°S, 41°W) and station B (74.1°S, 42°W) in the first-year ice of the Weddell Sea. Arrows indicate when air temperature dropped below −4.7°C [see (C)], the temperature at which brine volume decreases below the threshold necessary for nutrient exchange within the ice sheet. (**B**) Magnitude of growth limitation induced by both light and nutrients (the lowest value determines the most limiting resource) in the freeboard layer at station B. The gray area denotes the range of values and the thick line denotes the mean for the nutrient limitation term at the nine grid points comprising station B The steep decline in primary productivity shown in (A) at station B in late February resulted from the drop in the nutrient limitation term to zero in many of the grid points (the mean value was 0.42). A similar decline in primary productivity was not observed in late December, when the mean nutrient limitation term was similarly low (0.41), because the nutrient limitation term in all subsectors of station B exhibited values greater than zero. (**C**) Surface air temperatures at stations A and B. (**D**) Primary production in the infiltration layer at stations A and B. (**E**) Magnitude of growth limitation induced by light and nutrients in the infiltration layer at station B.

mand until early February (Fig. 3E). Consequently, primary production was restricted to locations that were submerged and suffused with nutrients, which amounted to 15 to 25% of the total ice area (*12*). The infiltration layer became light-limited after February as sun elevation decreased and the nutrient demand of the diminishing algal community declined.

The annual rate of primary production within the Antarctic ice pack was calculated to be ~35.7 Tg C year^{-1} (*13*), consistent with other estimates of 30 to 70 Tg C year^{-1} (*9*, *14*). First-year ice accounted for 75% of annual primary production within the pack. Nearly 60% of annual production took place between November (11.5 Tg C), when sea ice was near its maximum extent (Fig. 2), and December (9.80 Tg C), when the rate of production per unit area was near its peak. The Weddell Sea accounted for ~50% of the annual production (15.8 Tg C) because of its extensive ice coverage and high rate of carbon fixation (Fig. 2). The most productive region of the Weddell Sea was located within the first-year ice near the eastern margin of the multiyear ice, along 45°W (Fig. 2). Snow remained relatively deep at this location throughout the spring and summer, resulting in frequent surface flooding, which provided nutrients to the infiltration algal communities. Together, the Weddell Sea, the Ross Sea (7.73 Tg C), and the southern Indian Ocean (6.66 Tg C) accounted for 85% of the annual production in Antarctic sea ice. Production in the Ross Sea was slightly higher than in the southern Indian Ocean because of its more extensive multiyear ice.

Our production estimate of 35.7 Tg C year^{-1} for Antarctic sea ice is about 1 to 4% of the annual biogenic carbon production in the Southern Ocean, estimated to be 980 to 3620 Tg C year^{-1} (*14*, *15*). However, our estimate of sea ice primary production is 9 to 25% of total production in the ice-covered Southern Ocean (including the highly productive marginal ice zones), which ranges from 141 to 383 Tg C year^{-1} (*9*, *15*). Although sea ice primary production represents a small part of the Southern Ocean production, it is important as a highly concentrated food source for zooplankton such as juvenile krill (*4*), whose total carbon biomass in ice-covered waters (*16*) is <10% of the calculated annual production in sea ice.

The ability to resolve primary productivity differences in diverse pack ice habitats (for example, first-year versus multiyear ice, infiltration versus freeboard layer) is critical to assessing the response of the sea ice ecosystem to future changes in environmental conditions. For example, although atmospheric temperature is positively correlated with precipitation, it is negatively correlated with multiyear ice extent (*17*). Our model results suggest that an increase in snow cover or a decrease in the proportion of multiyear ice in response to climate warming would result in enhanced primary production within the Antarctic ice pack. However, at some point, the light-limiting effects of a thickening snow cover would outweigh the benefits of an increased nutrient supply resulting from flooding. In addition, if warming increased to the extent that the amount of first-year ice was reduced, the sea ice primary production would decrease accordingly.

REFERENCES AND NOTES

1. H. J. Zwally *et al.*, *Antarctic Sea Ice, 1973–1976: Satellite Passive Microwave Observations* (SP-459, NASA, Washington, DC, 1983).
2. K. R. Arrigo *et al.*, *Mar. Ecol. Prog. Ser.* **98**, 173 (1993).
3. K. R. Arrigo *et al.*, *ibid.* **127**, 255 (1995).
4. J. J. Stretch *et al.*, *ibid.* **44**, 131 (1988).
5. The model includes (i) atmospheric spectral radiation (400 to 700 nm) as a function of time, date, latitude, and cloud cover; (ii) in-ice bio-optics; (iii) sea ice geophysics; and (iv) biological dynamics. Algal production was calculated at each vertical grid point as a function of temperature, brine salinity, photosynthetically usable radiation, and nutrients. Algal accumulation was reduced by a loss term that included the effects of death, zooplankton grazing, and sinking. Additional details can be found in (*6*) and (*7*). The model grid is based on the special sensor microwave/imager (SSM/I) with a horizontal resolution of 625 km^2. The infiltration and internal freeboard layers were 0.02 m and 0.10 m thick, respectively. A uniform ice layer (0.10 m thick) separated the infiltration and freeboard layers. Layer thicknesses were held constant for the length of the integration. Ice thickness below the freeboard layer was variable and was used to distinguish first-year from multiyear ice. First-year ice had a total thickness of 0.75 m, whereas the thickest multiyear ice was 1.50 m. The initial distribution of multiyear ice was determined from the minimum ice extent in February 1989. The model was initialized on 1 October 1989 with a uniform chlorophyll a concentration of 1 mg m^{-3}. During the integration period, any multiyear ice that disappeared and then reappeared did so as first-year ice, with an initial chlorophyll a concentration of 1 mg m^{-3}. The model was run with 1-hour time steps at a vertical resolution of 0.5 cm in the infiltration layer and 1 cm in the freeboard layer.
6. K. R. Arrigo *et al.*, *J. Geophys. Res.* **98**, 6929 (1993).
7. K. R. Arrigo and C. W. Sullivan, *Limnol. Oceanogr.* **39**, 609 (1994).
8. In the infiltration layer, nutrients were supplied continuously whenever the snow density and thickness were sufficient to force the sea ice below sea level (the ice surface flooded). Nutrients were supplied to the interior freeboard layer when sea ice brine volume, a function of temperature and sea ice salinity, exceeded 70 per mil (the sea ice became permeable) as well as when the surface flooded. If these criteria were not met, the nutrient supply was cut off until the surface flooded or the ice became permeable again.
9. L. Legendre *et al.*, *Polar Biol.* **12**, 429 (1992).
10. The model uses as input the daily sea ice concentrations derived from SSM/I. The model calculates productivity at pixels where sea ice concentration exceeds 50%. Maps of snow distribution were generated from SSM/I imagery (*18*). Because horizontal variability of snow thickness within the 625-km^2 SSM/I pixel is substantial, subpixel variation in snow thickness was simulated by creating nine equal area grid points per pixel. The snow thickness at each grid point was calculated by multiplying the snow depth for that pixel by one of nine multipliers. These multipliers (0.272, 0.532, 0.952, 1.74, 3.308, 1.305, 0.721, 0.427, and 0.102) were chosen so that the distribution of snow thickness within each 625-km^2 pixel was consistent with the log-normal frequency distribution observed in situ. The multiplier applied to a given grid point was shifted at most one step to the right or left of the previous multiplier in the array every 4 days to simulate temporal changes in snow thickness at each grid point. The array was ordered such that the difference between adjacent elements was minimized, which ensured that temporal changes in snow thickness at each grid point were not too abrupt. For example, after a multiplier of 0.721 was applied to a grid point, the potential multipliers that could be applied subsequently were 1.305, 0.721, or 0.427, with the actual multiplier chosen at random. Production was calculated independently for each grid point, and all grid points within a pixel were averaged to obtain the productivity for that pixel. Spatial variation in nutrient concentrations within seawater, which supplies the sea ice, were obtained from annual climatologies (*19*). Seawater salinity was obtained from (*20*). Cloud cover, sea-level air pressure, relative humidity, and sea-level air temperature used in the atmospheric model were obtained from (*21*). Total column ozone was calculated as the averaged monthly climatologies from years 1989 to 1991 of the total ozone mapping spectrometer data. Total column precipitable water was calculated as the averaged monthly climatologies from years 1985 to 1988 of the TIROS operational vertical sounder data. All monthly climatologies were interpolated daily during the model integration.
11. Over most of the Antarctic ice pack, maximum productivity in the freeboard layer was approximately uniform and close to 1 g C m^{-2} month^{-1}. However, because sea ice in the southwestern Pacific Ocean was constantly disappearing and reforming (on average, sea ice at a given location there attained a maximum age of 20 days), rates of production in the freeboard layer were ~50% lower than in the rest of the ice pack.
12. Similar proportions of submerged sea ice in the Weddell Sea were reported by P. Wadhams *et al.* [*J. Geophys. Res.* **92**, 14535 (1987)].
13. Our estimate of primary production within sea ice must be considered conservative. Pack ice consists of ice of varied age, thickness, diameter, and structural irregularities (for example, rafted ice floes, snow drifts, and refrozen leads), which adds to the potential sites for algal colonization and may result in higher estimates of production.
14. S. Mathot *et al.*, *Eos* **76** (no. 3), OS143 (1996).
15. W. O. Smith and D. M. Nelson, *Bioscience* **36**, 251 (1986).
16. T. K. Frazer, L. B. Quetin, R. M. Ross, in *Antarctic Communities: Species, Structure and Survival*, B. Battaglia, J. Valencia, D. W. H. Walton, Eds. (Cambridge Univ. Press, Cambridge, 1997), pp. 107–111.
17. S. S. Jacobs and J. C. Comiso, *Geophys. Res. Lett.* **20**, 1171 (1993).
18. K. R. Arrigo *et al.*, *NASA Tech. Memo. 104640* (1996).
19. M. E. Conkright *et al.*, *World Ocean Atlas 1994*, vol. 1, *Nutrients* (NOAA Atlas NESDIS 1, U.S. Department of Commerce, Washington, DC, 1994).
20. S. Levitus *et al.*, *World Ocean Atlas 1994*, vol. 3, *Salinity* [National Oceanic and Atmospheric Administration (NOAA) Atlas NESDIS 3, U.S. Department of Commerce, Washington, DC, 1994].
21. A. M. da Silva, C. C. Young, S. Levitus, *Atlas of Surface Marine Data 1994*, vol. 1, *Algorithms and Procedures* (NOAA Atlas NESDIS 6, U.S. Department of Commerce, Washington, DC, 1994).

22. We thank S. Fiegles for assistance with SSM/I imagery; S. Ackley, D. Robinson, and C. Fritsen for helpful discussions and technical advice; and W. Olson, C. McClain, W. Esaias, L. Harding, and A. Schnell for editorial comments. Supported by NSF grant OPP 95-25805 (K.R.A. and M.P.L.) and NASA grants 971-438-20-10 and 971-148-65-56 (K.R.A.).

10 September 1996; accepted 14 February 1997